Impact of Halogen Axial Coordination on the Electronic and Magnetic Properties of MN_4 Single-Atom Catalysts for Oxygen Reduction

Bo-Yang Luo[‡,a,b], Chen Li[‡,b], Yu-Mei Yang [b], Wei Du [a] & Ya-Min Wang [a]*

[a.] School of Biological & Chemical Engineering, Zhejiang University of Science and Technology, Hangzhou 310023, Zhejiang, China.

[b.] School of Mechanical & Energy Engineering, Zhejiang University of Science and Technology, Hangzhou 310023, Zhejiang, China.

‡ These authors contributed equally to this work.

* Email: wangym@zust.edu.cn (Y.M.W)

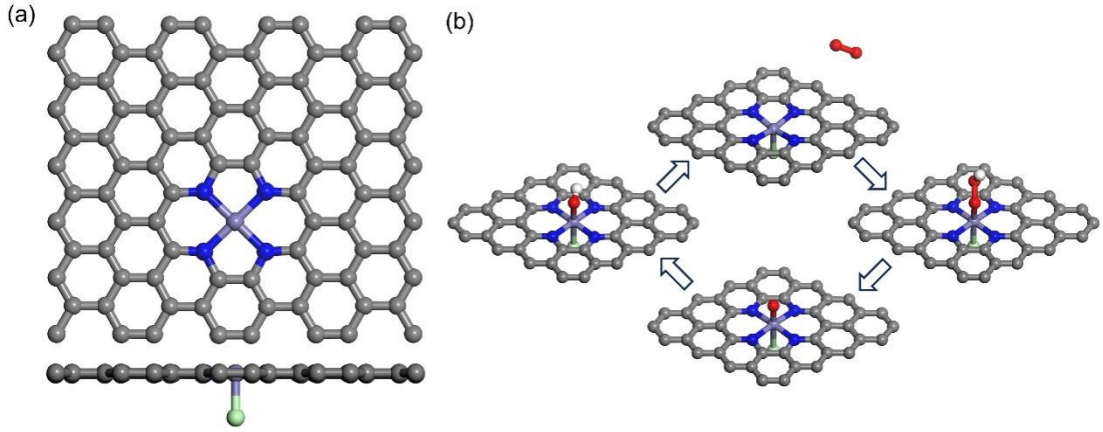

Figure S1. (a) Top and side views of the MN_4–X/C model. (b) Structural evolution of active site for MN_4–X /C in electrochemical ORR. Color codes: H in white; O in red; C in gray; N in blue; the single atom metal (M) in purple. The axial ligand (X) is schematically marked as the green ball.

The currently widely accepted theoretical approach for the ORR reaction is the four-electron transfer pathway in acidic media, as shown in the equation.

$$* + O_2 + H^+ + e^- \rightarrow *OOH \quad (1)$$

$$*OOH + H^+ + e^- \rightarrow *O + H_2O \quad (2)$$

$$*O + H^+ + e^- \rightarrow *OH \quad (3)$$

$$*OH + H^+ + e^- \rightarrow * + H_2O \quad (4)$$

In the equation, *, *OOH, *O, and *OH represent the adsorption sites and the adsorbed intermediates OOH, *O, and *OH, respectively. Based on the above four elementary steps, the corresponding Gibbs free energy (ΔG) can be obtained by:

$$\Delta G = \Delta E + \Delta E_{ZPE} - T\Delta S + \Delta G_{pH} + \Delta G_U \quad (5)$$

Where ΔE is the total reaction energy obtained from DFT calculations, ΔE_{ZPE} and ΔS are the

changes in zero-point energy and entropy, respectively. T is the temperature, set to 298.15K. ΔG_{pH} is the correction for the free energy of OH in alkaline media($\Delta G_{pH} = -k_B T ln H^+ = k_B \times pH \times ln10$, where k_B denotes the Boltzmann constant and pH was set to 0), and ΔG_U is the energy shift caused by the applied potential U ($\Delta G_U = -neU$), where n is the number of electrons transferred in the reaction and U is the applied electrode potential.

Therefore, based on the above free energy results, the limiting potential ($U_L = -\Delta G_{min}/e$), where ΔG_{min} is the step that releases the minimum energy among the four steps, i.e. the thermodynamic rate-determining step (RDS). The value of U_L closer to the ideal 1.23 V, the catalyst exhibits higher intrinsic activity.

Use the following equation to calculate the binding energy (E_b) between the substrate (MN_4/C) and the axial ligand X

$$E_b = E_{MN_4-X/C} - (E_{MN_4/C} + E_X) \tag{6}$$

Where $E_{MN_4-X/C}$, $E_{MN_4/C}$, and E_X represent the energies of the MN_4/C with the axial ligand, the MN_4/C without the axial ligand, and the axial ligand, respectively.

The adsorption strengths of the ORR intermediates (*OOH, *O, and *OH) were calculated at T=300 K, pH=0, and U=0 V (vs SHE) using to Eqs. (7)-(9), where * denotes the adsorption sites.

$$\Delta G_{*OOH} = G_{*OOH} + 3/2G_{H_2} - G_* - 2G_{H_2O} \tag{7}$$

$$\Delta G_{*O} = G_{*O} + G_{H_2} - G_* - G_{H_2O} \tag{8}$$

$$\Delta G_{*OH} = G_{*OH} + 1/2G_{H_2} - G_* - G_{H_2O} \tag{9}$$

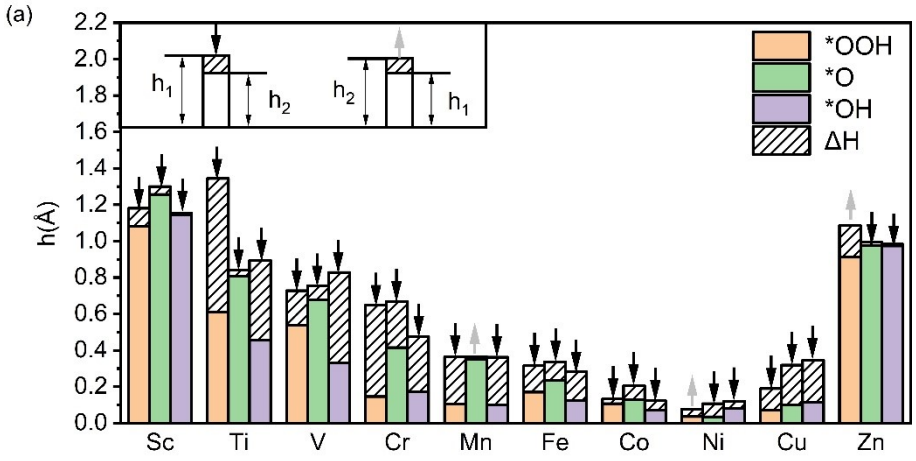

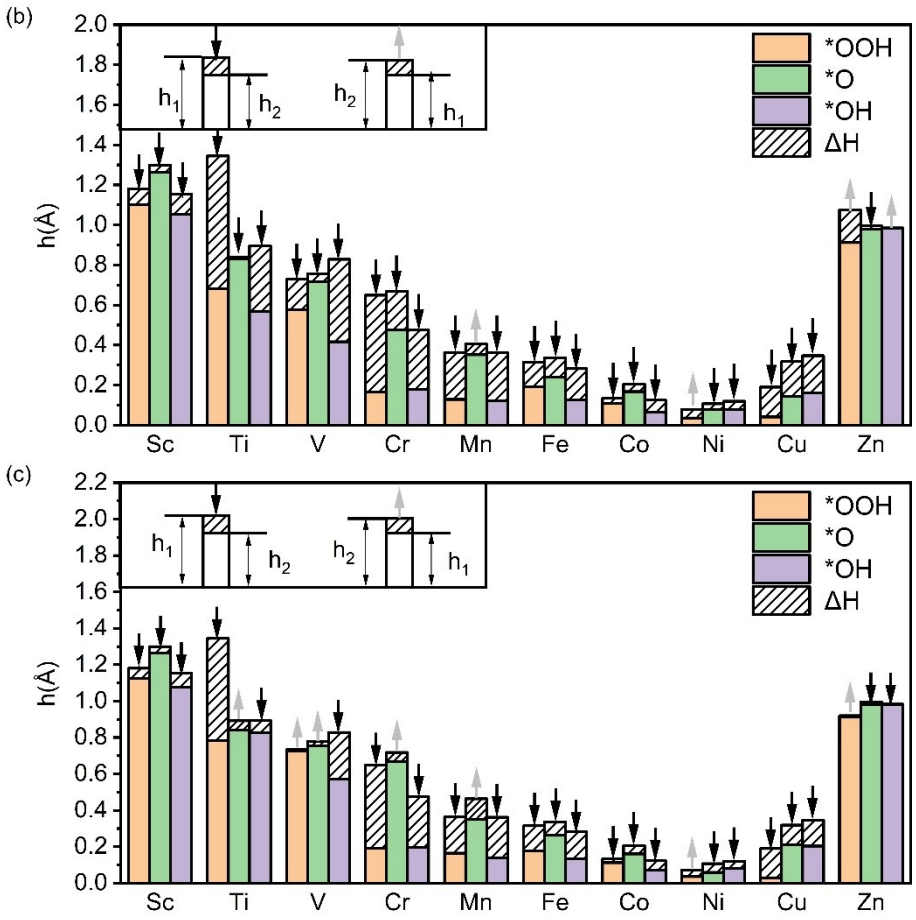

Figure S2. Height differential, denoted as $\Delta H = h_1 - h_2$ within the shaded regions, serves as an indicator of axial ligand effects. Here, h_1 and h_2 represent the vertical displacement of the metal atom from the surface during the oxygen reduction reaction (ORR) process. The difference in height ($\Delta H = h_1 - h_2$) is compared between MN_4/C and MN_4-Cl/C (a), MN_4-Br/C (b), and MN_4-I/C (c), respectively.

Table S1. The Gibbs free energy (ΔG, eV) for each elementary step of the ORR process on MN_4/C catalysts. The step shown in **bold** denotes the rate-determining step (RDS).

	ΔG_1	ΔG_2	ΔG_3	ΔG_4
ScN_4/C	-3.72	-0.92	-1.33	**1.05**
TiN_4/C	-6.35	-1.04	-0.03	**2.50**
VN_4/C	-4.15	-2.84	0.48	**1.59**
CrN_4/C	-2.32	-2.62	-0.11	**0.13**
MnN_4/C	-1.30	-2.25	-0.74	**-0.63**
FeN_4/C	-1.41	-2.15	-0.78	**-0.59**
CoN_4/C	-0.98	-1.28	-1.71	**-0.94**
NiN_4/C	**-0.03**	-0.54	-2.32	-2.02
CuN_4/C	**-0.09**	-0.53	-2.41	-1.90
ZnN_4/C	-0.86	**-0.73**	-2.51	-0.82

Table S2. The Gibbs free energy (ΔG, eV) for each elementary step of the ORR process on MN_4-

F/C catalysts. The step shown in **bold** denotes the rate-determining step (RDS).

	ΔG_1	ΔG_2	ΔG_3	ΔG_4
ScN_4-F/C	**0.69**	-0.48	-2.66	-2.47
TiN_4-F/C	**-0.51**	-2.20	-1.04	-1.18
VN_4-F/C	-0.74	-2.96	**-0.43**	-0.80
CrN_4-F/C	-0.92	-2.41	**-0.74**	-0.84
MnN_4-F/C	-1.19	-1.84	-1.35	**-0.54**
FeN_4-F/C	-1.16	-1.95	-1.05	**-0.76**
CoN_4-F/C	**-0.88**	-1.31	-1.74	-0.98
NiN_4-F/C	**-0.33**	-0.86	-2.12	-1.61
CuN_4-F/C	**0.22**	-0.51	-2.47	-2.17
ZnN_4-F/C	**0.19**	-0.17	-2.21	-2.73

Table S3. The Gibbs free energy (ΔG, eV) for each elementary step of the ORR process on MN_4-Cl/C catalysts. The step shown in **bold** denotes the rate-determining step (RDS).

	ΔG_1	ΔG_2	ΔG_3	ΔG_4
ScN_4-Cl/C	**0.02**	-0.89	-2.35	-1.71
TiN_4-Cl/C	-0.64	-2.70	**-0.51**	-1.08
VN_4-Cl/C	-0.64	-3.29	**-0.04**	-0.95
CrN_4-Cl/C	**-0.80**	-2.37	-0.80	-0.94
MnN_4-Cl/C	-1.02	-1.92	-1.25	**-0.73**
FeN_4-Cl/C	-1.04	-1.90	-1.06	**-0.91**
CoN_4-Cl/C	**-0.71**	-1.16	-1.88	-1.17
NiN_4-Cl/C	**-0.19**	-0.75	-2.12	-1.86
CuN_4-Cl/C	**0.15**	-0.53	-2.26	-2.27
ZnN_4-Cl/C	**0.20**	-0.26	-2.52	-2.34

Table S4. The Gibbs free energy (ΔG, eV) for each elementary step of the ORR process on MN_4-Br/C catalysts. The step shown in **bold** denotes the rate-determining step (RDS).

	ΔG_1	ΔG_2	ΔG_3	ΔG_4
ScN_4-Br/C	**-0.26**	-0.92	-2.28	-1.46
TiN_4-Br/C	-0.77	-2.82	**-0.37**	-0.95
VN_4-Br/C	-0.72	-3.40	**0.10**	-0.89
CrN_4-Br/C	-0.83	-2.40	**-0.76**	-0.93
MnN_4-Br/C	-0.93	-2.06	-1.16	**-0.76**
FeN_4-Br/C	-1.01	-1.92	-1.06	**-0.93**
CoN_4-Br/C	**-0.68**	-1.14	-1.89	-1.20
NiN_4-Br/C	**-0.15**	-0.66	-2.19	-1.92
CuN_4-Br/C	**0.13**	-0.53	-2.28	-2.24
ZnN_4-Br/C	**0.11**	-0.35	-2.52	-2.15

Table S5. The Gibbs free energy (ΔG, eV) for each elementary step of the ORR process on MN_4-

I/C catalysts. The step shown in **bold** denotes the rate-determining step (RDS).

	ΔG_1	ΔG_2	ΔG_3	ΔG_4
ScN_4-I/C	**-0.63**	-0.93	-2.26	-1.09
TiN_4- I /C	-0.99	-2.94	**-0.26**	-0.73
VN_4- I /C	-0.94	-3.51	**0.24**	-0.70
CrN_4- I /C	-0.83	-2.63	**-0.53**	-0.92
MnN_4- I /C	-0.89	-2.10	-1.09	**-0.83**
FeN_4- I /C	**-0.96**	-1.93	-1.06	-0.97
CoN_4- I /C	**-0.62**	-1.12	-1.91	-1.28
NiN_4- I /C	**-0.13**	-0.69	-2.14	-1.96
CuN_4- I /C	**0.11**	-0.53	-2.29	-2.21
ZnN_4- I /C	**0.38**	-0.76	-2.53	-2.01

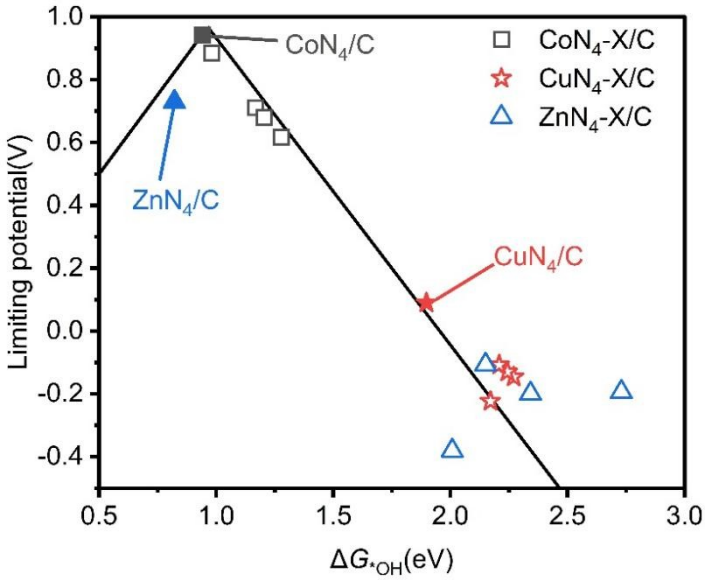

Figure S3. The volcano plot for the ORR limiting potential against the adsorption free energy of ΔG_{*OH} on MN_4/C and MN_4-X/C catalysts (M = Co, Cu, Zn; X = -F, -Cl, -Br, -I).

CoN_4/C**:** Its pristine form is already very close to the volcano peak. Therefore, the halogen-induced rightward shift is small but sufficient to move it slightly past the peak onto the right leg, resulting in minimal or slightly negative activity change.

CuN_4/C and ZnN_4/C**:** Our supplemental analysis indicates their pristine forms are already located *clearly on the right leg* of the volcano, far from the peak. The halogen-induced rightward shift therefore moves them even further away from optimal activity.

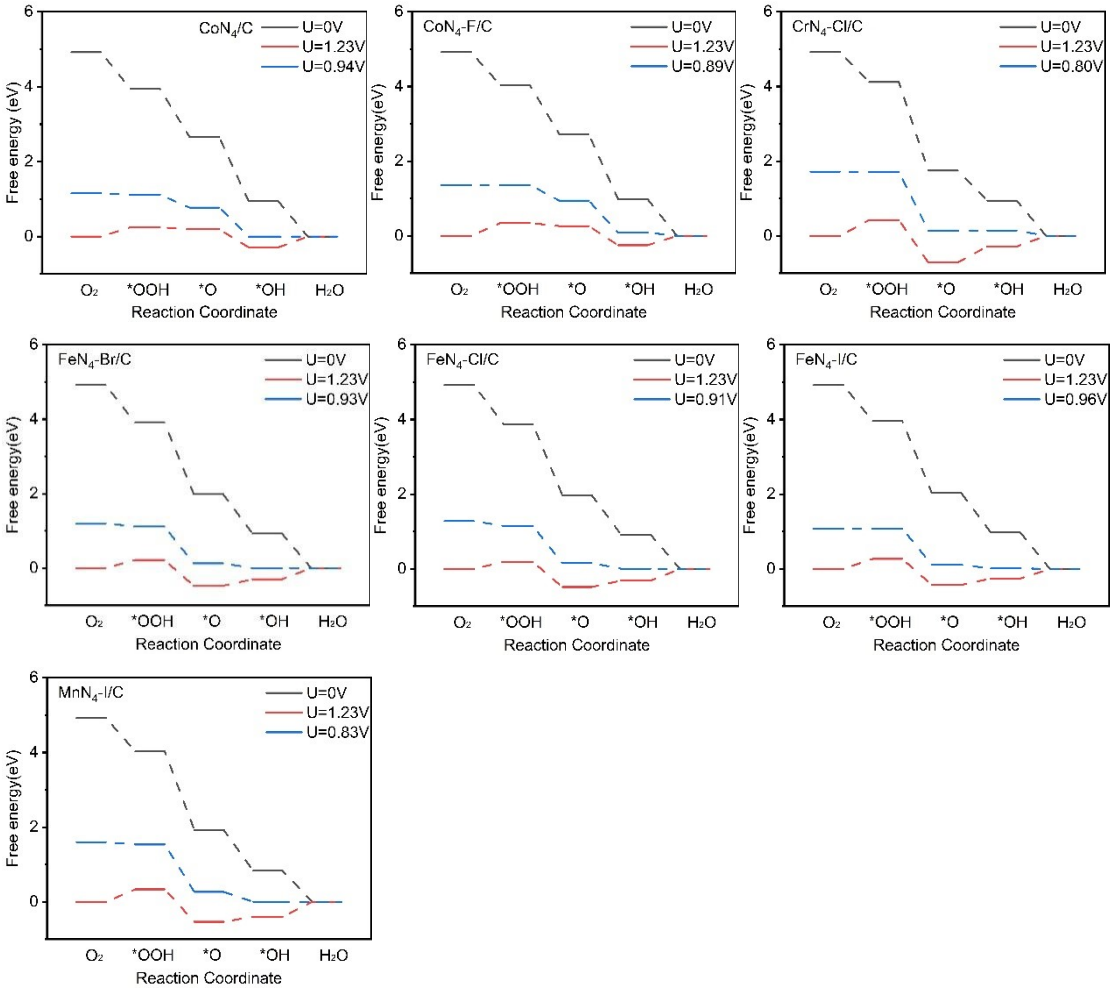

Figure S4. The ORR free energy diagrams for these seven promising candidates.

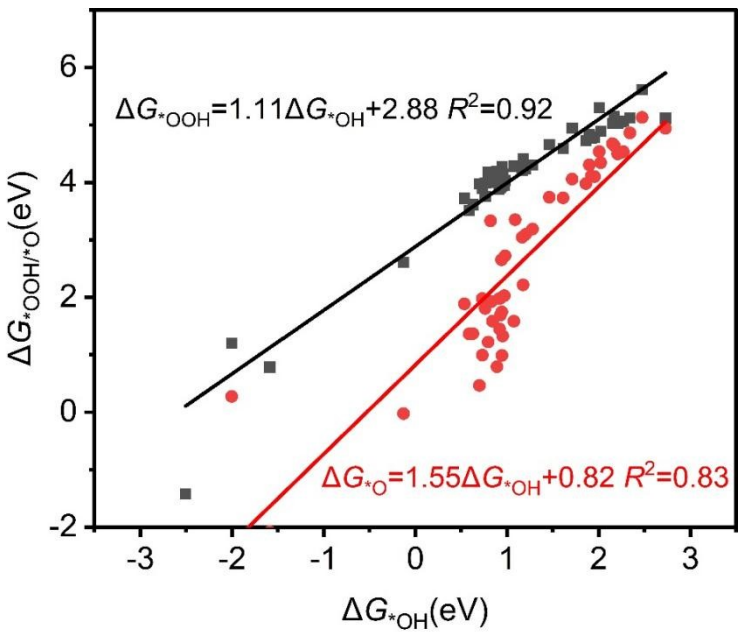

Figure S5. The scaling relations of ΔG_{*OOH} vs. ΔG_{*OH} and that of ΔG_{*O} vs. ΔG_{*OH} for all the pristine MN_4/C and axial ligand engineered MN_4-X/C models.

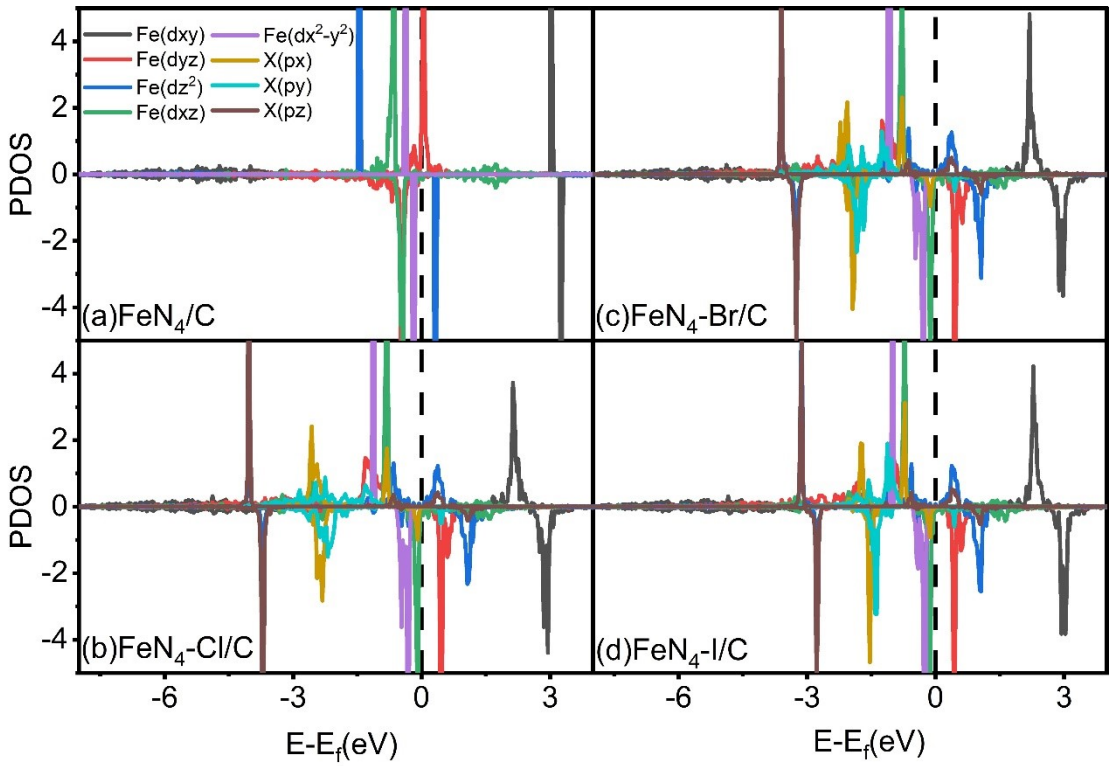

Figure S6. The projected density of states (PDOS) diagrams are presented for: a) FeN_4/C, b) FeN_4-Cl/C, c) FeN_4-Br/C, d) FeN_4-I/C. Herein, X represents the axially modified halogen ligand.

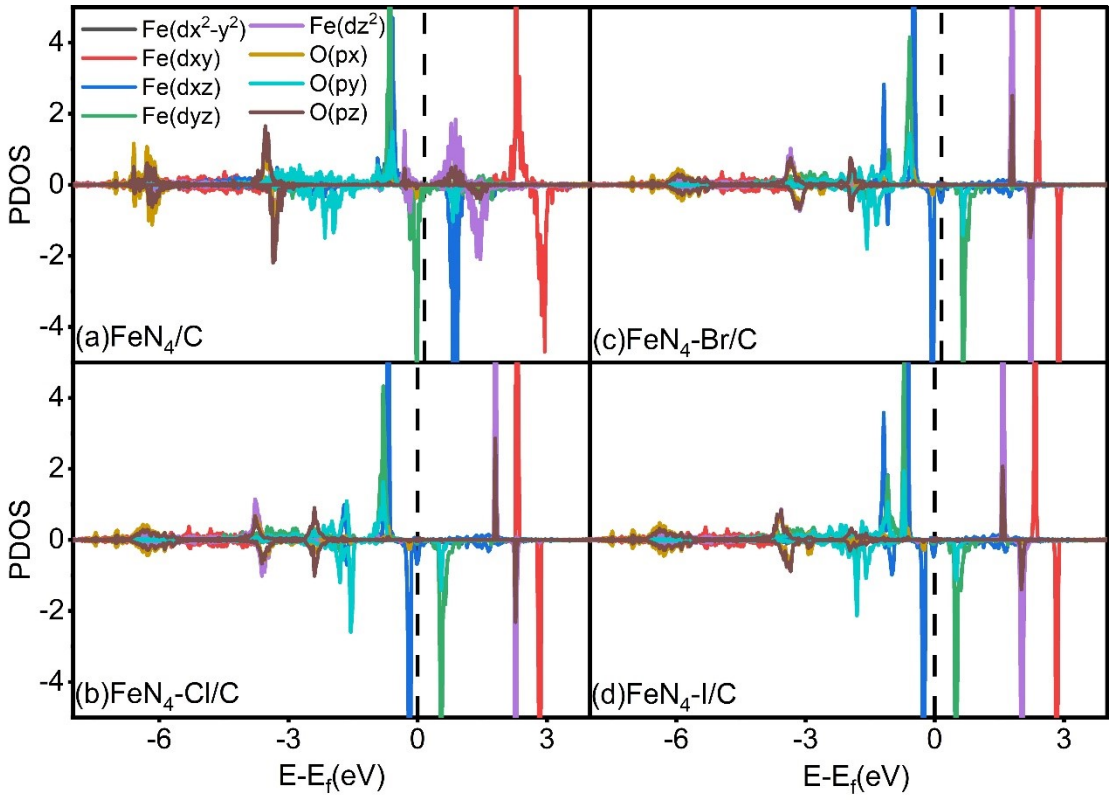

Figure S7. The projected density of states (PDOS) diagrams are presented for: a) FeN_4/C, b) FeN_4-

Cl/C, c) FeN_4-Br/C, d) FeN_4-I/C. Here, O denotes the oxygen atom on the *OH intermediate of ORR.

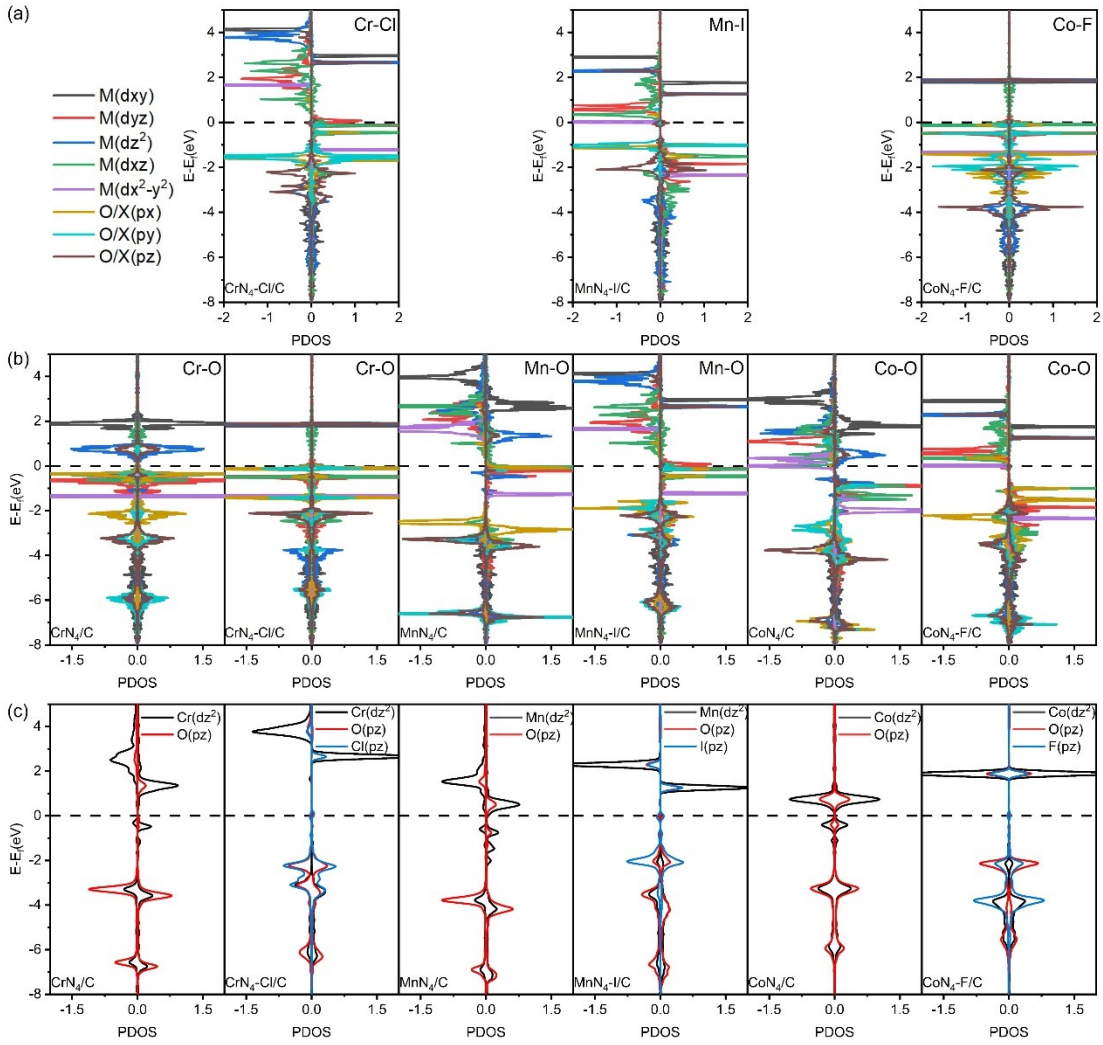

Figure S8. The projected density of states (PDOS) analysis for CrN_4/C, CrN_4-Cl/C, MnN_4/C, MnN_4-I/C, CoN_4/C, and CoN_4-F/C catalysts, elucidating the electronic interaction between the metal center, axial halogen ligand, and adsorbed *OH intermediate.

In panels S8a and S8b, the bonding characteristics are detailed via the PDOS of metal d-orbitals, halogen p-orbitals (for M–X bonding), and oxygen p-orbitals (for M–*OH bonding). The key insight is provided in Figure S8c, which focuses on the PDOS overlap between the metal dz^2 orbital and the O pz orbital of OH. Upon introduction of an axial halogen ligand, the energy level of the metal dz^2–O pz overlap shifts upward. This shift indicates a weakening of the metal–OH interaction, which is attributed to the competitive occupancy of the metal dz^2 orbital between the halogen p-orbital and the *OH species.

This electronic weakening effect directly explains the trends observed in the activity volcano plot (Figure S3). For CoN_4/C, which initially lies near the volcanic peak, the halogen-induced weakening mildly shifts ΔG_{*OH} to the right, resulting in minimal activity change. In contrast, for CuN_4/C and ZnN_4/C—already situated on the right leg of the volcano—the same weakening further increases ΔG_{*OH}, moving them farther from the optimal *OH binding strength and thus reducing their ORR

activity. Therefore, Figure S8 provides a fundamental electronic-structure basis for the halogen-mediated modulation of *OH adsorption and the resulting ORR performance.

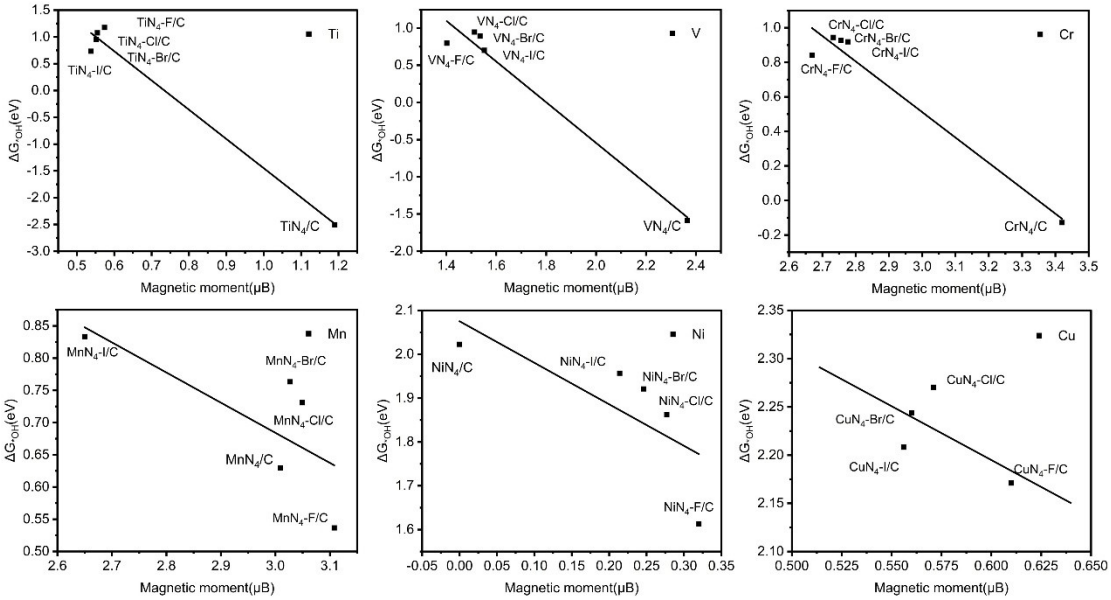

Figure S9. Magnetic moment vs. $\Delta G_{*\mathrm{OH}}$ scaling relations. A lower magnetic moment correlates with weaker adsorption of the *OH intermediate across the studied M-N-C catalysts. Data for the full Sc–Zn series are provided in Table S6. Regarding the cases of Sc, Co, and Zn—which were not emphasized initially—it is important to note that after axial modification, these systems exhibit notably weak or even non-magnetic behavior. As further illustrated in the newly added Figure SX (Paper V2), the calculated magnetic moments across the ten transition-metal catalysts (Sc to Zn) display a volcano-shaped trend, with Sc and Zn showing zero magnetic moments, while Mn occupies the peak position. This observation aligns with findings reported in prior studies on transition metal monoxides[1].

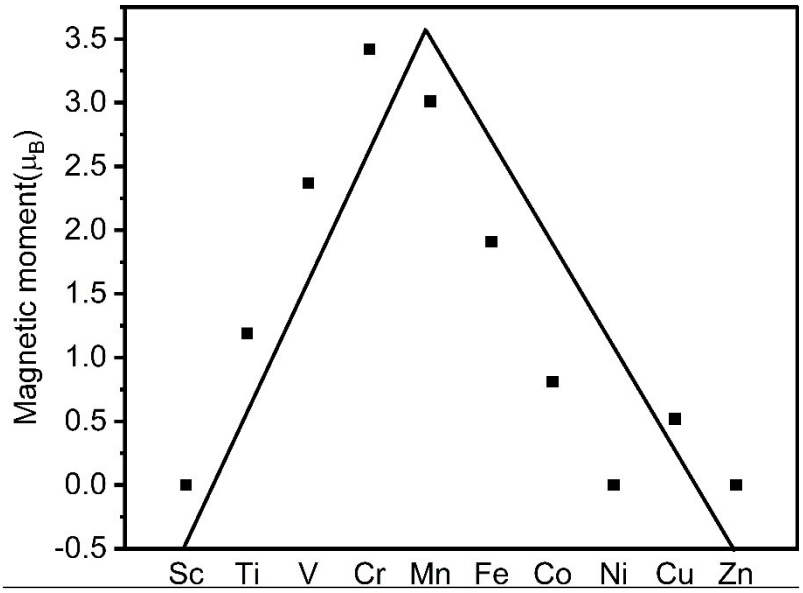

Figure S10. Computed magnetic moment of transition metals in MN_4/C catalysts.

Table S6. The magnetic moments (m, μB) at the metal centers in M-N-C catalysts. Systems highlighted in bold denote either the top-performing catalysts or the corresponding non-engineered benchmarks for comparison.

	Sc	**Ti**	**V**	**Cr**	**Mn**	**Fe**	**Co**	**Ni**	**Cu**	**Zn**
MN_4/C	0.00	1.19	2.37	**3.42**	**3.01**	**1.91**	**0.81**	0.00	0.52	0.00
MN_4-F/C	0.00	0.57	1.40	2.67	3.11	**1.70**	**0.00**	0.32	0.61	0.00
MN_4-Cl/C	0.00	0.56	1.51	**2.73**	3.05	**1.33**	0.00	0.28	0.57	0.00
MN_4-Br/C	0.00	0.55	1.54	2.76	3.03	**1.31**	0.00	0.25	0.56	0.00
MN_4-I/C	0.00	0.54	1.55	2.78	**2.65**	**1.26**	0.00	0.21	0.56	0.00

Reference

1 J. Liu, T. Yang, A. Xu, R. L. Martin, Y. Yang, H. Jiao, Y. Li and X.-D. Wen, *J. Alloys Compd.*, 2019, **808**, 151707.